Radiation source displacement measurement based on spatial resolution characteristics of active pixel sensors*

Shou-Long Xu,[1] Yu-Bo Wang,[1] Qing-xin Li,[1] Zhi-Ling Wang,[1] Zhi-Xiong Hou,[1] Cui-Yue Wei,[1] and Yi-Jun Zhong[1,†]

[1]*University of South China, Hengyang, Hunan 421001, China*

In this paper, we leverage the high spatial resolution and strong sensitivity to charged particles of CMOS sensors by employing the weighted centroid method to determine the displacement direction and position of radiation sources, and we evaluate its effectiveness in locating moving radiation sources. Additionally, we investigated the morphological characteristics of α-particle response signals and analyzed the response uniformity and sensitivity of different sensor regions under the influence of a collimating structure. The results indicate that the α-particle response signal is characterized by a concentration of high pixel value pixels, with 3–8 pixels having pixel values between 150 and 255. The sensor regions demonstrated highly consistent responses during irradiation, indicating high sensitivity to changes in the radiation source position. The peak non-uniformity value in the irradiated central region did not exceed 0.125, the non-uniformity difference between regions at the same distance was less than 0.025, and the non-uniformity of each region gradually decreased with increasing distance from the irradiated center.Compared to the classical centroid localization method, the weighted centroid method significantly improved localization accuracy and stability. Localization error gradually converged as the number of accumulated frames increased, reaching approximately 8 pixels when the number of accumulated frames reached 100. Furthermore, when tracking the continuously moving radiation source, the predicted path closely matched the actual path, with the error in the predicted centroid displacement speed being less than 5% compared to the actual speed.

Keywords: CMOS sensor, radiation source localization, weighted centroid method, real-time dynamic tracking

INTRODUCTION

Pixel sensors, renowned for their exceptional spatial resolution, hold significant potential and value in nuclear radiation measurement and nuclear technology applications. In recent years, numerous scholars have investigated ionizing radiation detection using CMOS active pixel sensors, confirming their effectiveness in detecting ionizing particles [1–3]. These studies also demonstrate that CMOS sensors maintain uniform temporal and spatial responses under steady radiation fields [4–7]. Almeida [8] and colleagues evaluated the noise characteristics of CMOS sensors in the CYGNO experiment, verifying the sensors' high spatial resolution and excellent noise suppression capabilities in low radiation backgrounds. Ren [9] and his team developed a CMOS sensor based on the Time-Over-Threshold (ToT) technique, which accurately captures the energy loss information of particles in high-energy physics experiments, significantly enhancing the spatial resolution of particle tracks. Bugiel [10] et al. utilized Silicon-On-Insulator (SOI) technology to improve the spatial resolution of CMOS sensors to 1.5 microns while maintaining high detection efficiency and radiation resistance, thereby achieving very high precision in particle tracking for high-energy physics experiments. Moustakas [11] and colleagues developed a monolithic active pixel sensor (MAPS) suitable for high-radiation environments, attaining a spatial resolution of approximately 10 microns through a small collecting electrode design. Mauro [12] et al. designed and fabricated a monolithic active pixel sensor based on 65 nm CMOS technology and conducted comprehensive performance evaluations, ultimately achieving a spatial resolution of less than 5 microns.

In terms of measurement capabilities, the spatial resolution and radiation sensitivity of CMOS active pixel sensors make them highly suitable for non-contact displacement measurement technologies, offering superior anti-interference capabilities compared to traditional displacement measurement methods. While machine learning and neural network algorithms can leverage detection data from these sensors for radiation source identification and localization in complex environments [13, 14], their training processes are complex, and real-time processing demands substantial computational resources, thereby increasing system complexity and resource consumption. In contrast, the weighted centroid algorithm assigns different weights to signals and estimates positions based on received signal strength, offering advantages such as simple computation and excellent real-time performance. Kumar [15] and colleagues proposed a radiation source localization method using particle filter algorithms combined with weighted centroid estimates of candidate location centers. This approach significantly improved localization accuracy through particle filtering and data fusion. Smith [16] et al. designed a gamma radiation source localization system for micro aerial vehicles (MAVs), successfully estimating the locations of gamma radiation sources by integrating the weighted centroid algorithm with event data captured by miniature Compton cameras. In the detection of weak radiation sources, Lee [17] and colleagues investigated how the weighted centroid algorithm could enhance detection sensitivity. By optimizing weights and determining the optimal detection window, their research demonstrated that under high background noise conditions, the weighted centroid method significantly improves both the detection sensitivity and localization accuracy of weak radiation sources.

* National Natural Science Foundation of China (11905102).

† Yi-Jun Zhong, zhongyijun152@126.com

This paper proposes a novel method for determining and measuring the displacement of radiation sources. Through radiation response experiments, we examined the global response capability of the CMOS APS pixel array. Based on the morphological characteristics of radiation response events and the distribution features of response signals under the influence of a collimating structure, we introduced a density parameter-based clustering algorithm. We proposed a method for determining and measuring radiation source displacement and experimentally validated radiation source localization, displacement direction determination, and measurement accuracy. The findings presented in this paper not only offer new methods and techniques for radiation source localization and non-contact displacement measurement but also expand the application market for ^{241}Am isotope radiation sources.

I. EXPERIMENTAL PREPARATION

A. Experimental Samples and Conditions

The experiment utilized a SONY MT9P031 active pixel sensor, featuring a pixel size of $2.2\,\mu m \times 2.2\,\mu m$ and an effective resolution of 2592 horizontal by 1944 vertical pixels, covering an active area of $6\,\mathrm{mm}\,(\mathrm{H}) \times 4\,\mathrm{mm}\,(\mathrm{V})$. The sensor supports 8–10 bit digital signal output. To ensure consistent and clear response signals, the sensor's gain was fixed at 50 dB, and the integration time was set to 45 ms. The glass protective layer on the sensor surface was removed to allow alpha rays (α rays) to penetrate the silicon pixel array. Data acquisition and processing were performed using the iCamera 51 microcontroller, with image data transmitted from the sensor module to the PC via a high-speed USB interface at a sampling frequency of 25 Hz.

This study employed a ^{241}Am alpha radiation source with a diameter of 2.13 mm, a characteristic alpha-ray energy of 5485.56 keV, and a radioactive activity of 29 kBq. In the absence of a collimating structure, the alpha particle flux rate on the sensor surface was $1.05 \times 10^4\ \mathrm{cm^{-2}s^{-1}}$. When a collimating structure was introduced, the flux rate decreased to $5.87 \times 10^3\ \mathrm{cm^{-2}s^{-1}}$. The experiments were conducted at room temperature, maintained at 25 °C.

A radiation source tracking platform was designed to facilitate the horizontal displacement of the radiation source, which was consistently positioned 5 mm above the sensor surface. A collimating structure was developed to produce a collimated and calibrated alpha-ray beam. The collimator featured a circular aperture with a diameter of 0.7 mm and a length of 1 mm. The experimental setup and test system are illustrated in Figure 1.

During the experiment, the top-left position was designated as the origin. A total of 500 image frames were collected, with the radiation source displaced by a specific distance between each acquisition for statistical analysis. The experimental scheme is detailed in Table 1. Figure 2 illustrates the movement path and the selection of irradiation points.

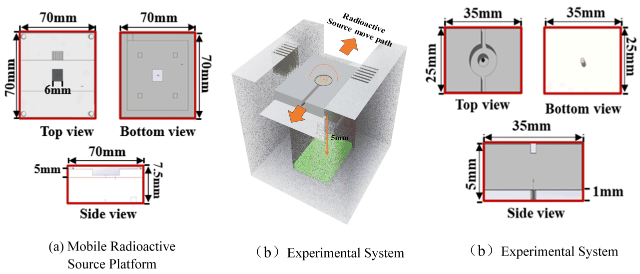

Fig. 1: Experimental System Diagram

Table 1: Experimental Scheme

Experiment No.	Starting Coordinates	Horizontal Displacement	Vertical Displacement
No.1	(2.7, 2.2)	0	0
No.2	(4.7, 0.5)	0	1
No.3	(0.7, 2.2)	1	0

B. Data Processing Methods

To calculate the rate of increase A_k of pixels within each pixel value interval and identify the interval most significantly affected by irradiation, the following formula is employed:

$$A_k = \frac{P_k^a}{P_k^b}$$

where P_k^a and P_k^b represent the proportion of pixels in the k-th pixel value interval before and after irradiation, respectively.

For pixels in various pixel value intervals, the proportion P_n of pixels in the eight neighboring pixels that belong to the same interval is calculated to assess the morphological characteristics of pixel aggregation:

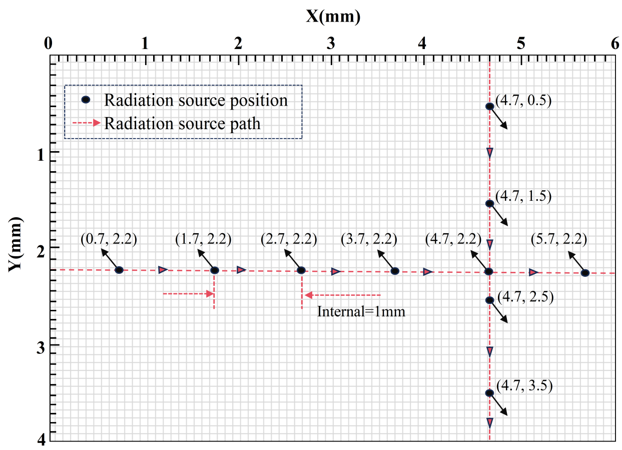

Fig. 2: Diagram of the Movement Path and Irradiation Point Selection

$$P_n = \frac{S_n}{S_j}$$

where S_n is the number of target pixels surrounded by eight neighboring pixels within the same pixel value interval, and S_j is the total number of target pixels in the pixel value interval $[g_k, g_{k+1}]$.

To evaluate the uniformity of the pixel array response and the morphological characteristics under the influence of a collimating structure, the entire CMOS active pixel sensor array is divided into 24 equal regions. Additionally, the signal-concentrated area is uniformly partitioned into five annular bands, as illustrated in figure 3.

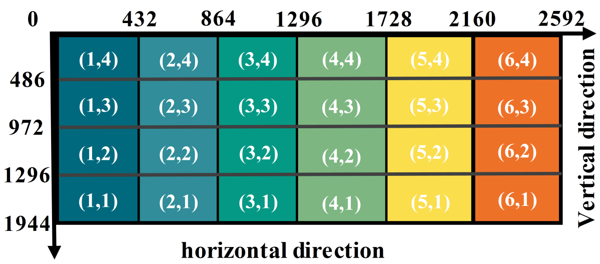

(a) Sensor Pixel Array Partitioning

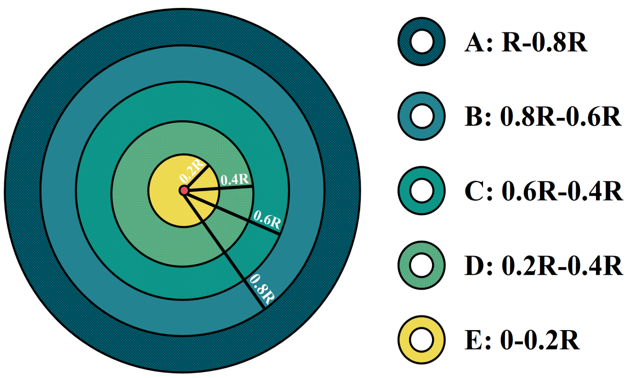

(b) Density Ring Band

Fig. 3: Pixel Array Region

To calculate the cumulative pixel value value E_i for each region to analyze the uniformity of the sensor's response when irradiating a specific region, the following formula is used:

$$E_i = \sum_{t=1}^{N} E_{ti}$$

where N is the total number of images, and $E_{t,i}$ is the pixel value value of region i in the t-th frame.

The non-uniformity R_{nud} of different regions in the pixel array represents the response differences between regions when the radiation source irradiates specific regions of the sensor:

$$R_{nud} = \frac{1}{S_i} \sqrt{\frac{1}{h} \sum_{n=1}^{h} (v_{xni} - S_i)^2}$$

where v_{xni} is the total pixel value of region i in the n-th image after moving the radiation source x mm, h is the total number of images, and S_i is the average pixel value of region i after a movement distance of x mm.

After overlaying the response signals from frames i to $i+k$ to construct a point set, annular regions are divided based on radii of $0.8d$, $0.6d$, $0.4d$, and $0.2d$, where d is the average distance from the boundary to the centroid. The signal concentration C within each band is calculated as:

$$C = \frac{N}{S}$$

where N is the number of response signals in the band, and S is the area of the band.

To analyze the error between the algorithm's localization results and the actual position of the radiation source, the average distance $\bar{d}$ between the weighted centroid and the actual irradiated position in the pixel array is calculated under different frame overlay counts:

$$\bar{d} = \frac{1}{N} \sum_{i=1}^{N} d_i = \frac{1}{N} \sum_{i=1}^{N} \sqrt{(x_{c_i} - x_r)^2 + (y_{c_i} - y_r)^2}$$

where N is the number of weighted centroid groups (i.e., the number of overlay frames), (x_{c_i}, y_{c_i}) is the coordinate of the weighted centroid in the i-th group, and (x_r, y_r) is the projected coordinate of the actual irradiated position.

II. EXPERIMENTAL RESULTS AND DISCUSSION

A. Global Response Analysis of the Pixel Array

Figure 4 presents three-dimensional scatter plots of the sensor's pixel value matrices before and after irradiation. In Figure 4a, the pixel value image before irradiation exhibits a relatively stable baseline formed by background noise. The pixel values are primarily distributed in the range of 0 to 50, with only a few noise peaks. This background noise mainly originates from the sensor's dark current and readout noise, which are inherent signals present when the sensor operates without external light or radiation.

In contrast, figure 4b shows the dark image during irradiation. It can be observed that many pixels exhibit significantly increased pixel values, although the number of pixels decreases as the pixel value increases. This phenomenon occurs because alpha particles—high-energy, positively charged helium nuclei—undergo strong ionizing collisions with atoms and electrons in the semiconductor material as they pass through it, rapidly depositing their energy over a very short distance.

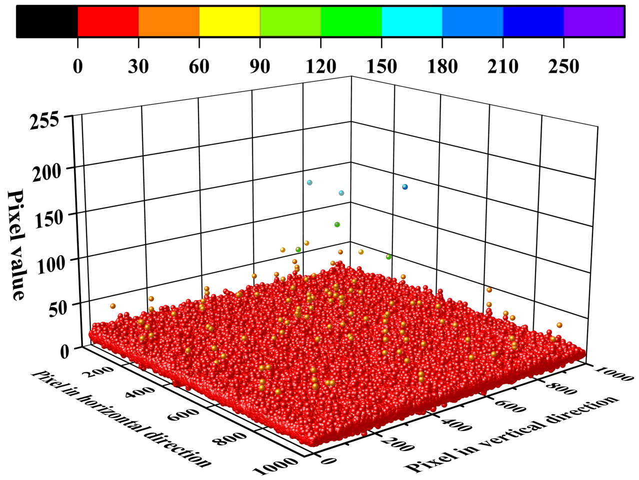

(a) Dark image of the pixel value matrix before irradiation

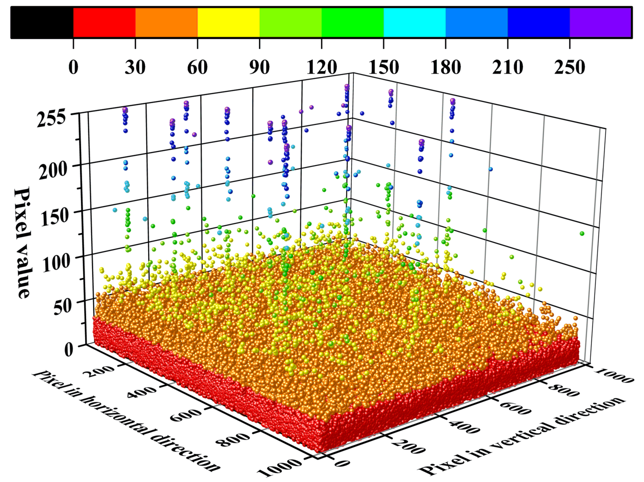

(b) Dark image of the pixel value matrix during irradiation

Fig. 4: 3D scatter plots of the pixel value matrix before and during irradiation

These collisions generate a large number of electron-hole pairs in the semiconductor material. As alpha particles traverse the sensor, the pixels along their paths produce strong electrical signals due to the substantial generation of electron-hole pairs, leading to significant increases in their pixel values. Because alpha particles have a short range (approximately tens of micrometers in solids), their impact is primarily concentrated in localized regions.

Table 2 presents the proportions of pixels in different pixel value intervals for 500 frames of images before and during irradiation. According to the statistical data, the proportion of pixels in the 50–100 interval increased by 34.6 times, in the 100–150 interval by 19 times, in the 150–200 interval by 47.3 times, and in the 200–255 interval by 25.5 times.

Table 2: Distribution of pixel values

Pixel Value Range	**Before Irradiation (%)**	**During Irradiation (%)**	**Increase Factor**
50 to 100	0.97×10^{-3}	0.33×10^{-1}	34.00
101 to 150	0.42×10^{-3}	0.80×10^{-2}	19.00
151 to 200	0.13×10^{-3}	0.61×10^{-2}	46.92
201 to 255	0.24×10^{-3}	0.55×10^{-2}	22.92

These results indicate that the energy deposition of alpha particles during irradiation significantly affects the pixel response of the sensor. In particular, in the 150–200 pixel value interval, the increase in the proportion of pixels is the largest, reaching 47.3 times. In summary, within this energy range, the impact of alpha particles on the sensor is the most significant.

B. Response Event Characteristics

Figure 5 presents the typical radiation event of the CMOS sensor exposed to the ^{241}Am α radiation source, depicted as a 3D bar chart and a heatmap. As shown in Figure 5a, the response is characterized by a sharp increase or saturation in the pixel values of multiple adjacent pixels in a specific region, while pixel value changes in other regions are relatively small. Consequently, the peak of the response event is relatively steep. This occurs because α particles deposit high energy in a specific region of the sensor, generating numerous electron-hole pairs. This leads to a rapid increase in the charge of adjacent pixels, forming a prominent pixel value peak. Meanwhile, other regions of the sensor are not directly irradiated, resulting in insignificant pixel value changes and a low noise level.

Although noise-induced variations in pixel gray values can fall within the same range as those caused by α particle events, the area affected by noise is smaller, generally involving only single pixels. This indicates that noise-induced pixel value changes are usually isolated and scattered, without forming prominent peak regions. Figure 5b shows the heatmap of pixel value distributions for α response events. During such an event, the gray values of multiple closely connected pixels significantly increase, forming concentrated areas of high gray values.

Figure 6 illustrates the proportion curves of pixel clusters for different gray value intervals. Under radiation, pixels with gray values in the 50–150 range have over 90% of their neighboring pixels containing only one or two pixels with similar gray values, while cases with three or more neighboring pixels in the same range account for less than 5%. This indicates that pixel distribution in this gray value interval is relatively scattered, lacking evident clustering characteristics. This dispersiveness mainly originates from background noise and the

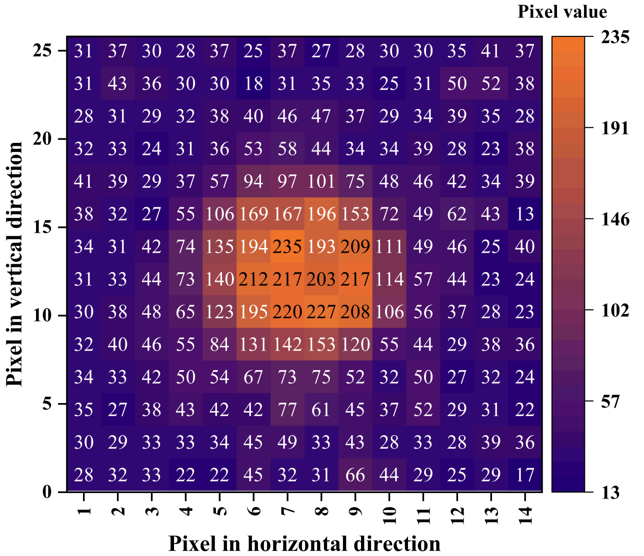

(a) Comparison between α response events and noise.

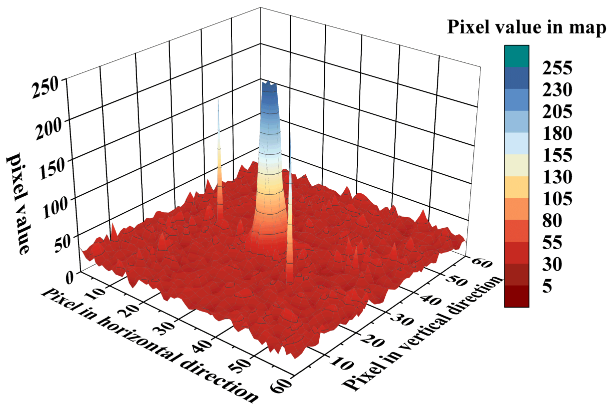

(b) Heatmap of Typical radiation events.

Fig. 5: Typical radiation events and the comparison between response events and noise

scattering of low-energy α particles within the material, leading to slight increases in individual pixel gray values that are insufficient to form continuous high-gray-value regions.

In contrast, pixels with gray values in the 150–255 range typically have more than three neighboring pixels within the same interval, showing highly concentrated distributions of high-gray-value pixels. This clustering is due to the strong ionization effects caused by α particles interacting with the sensor material. As α particles traverse the semiconductor material, they generate numerous electron-hole pairs along their paths, significantly elevating the gray values of adjacent pixels. Due to the short range of α particles, the deposited ionization charges easily enter the space charge regions of neighboring pixels, resulting in clusters of high-gray-value pixels forming circular spots.

Based on these characteristics, we utilize the spatial clustering property of high-gray-value pixels to identify and extract α particle response signals using a connected region algorithm. Specifically, pixels with gray values in the 150–255 range are selected as samples. The connected regions are constrained to contain between three and eight pixels to ensure that the extracted regions result from high-energy deposition by α particles rather than random noise or other factors. This approach enables the effective and high-precision extraction of α particle response signals from the image.

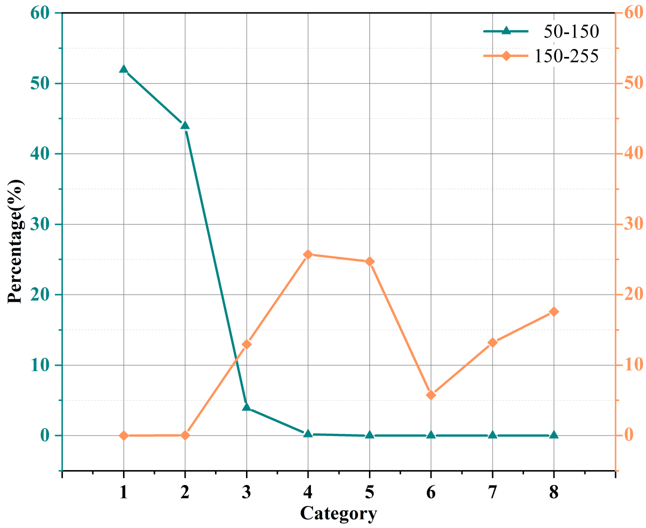

Fig. 6: Pixel Cluster Distribution

C. Analysis of the Response Signal Distribution Characteristics Under Collimating Structure Interference

Figure 7 illustrates the maximum ring radius of the response signal distribution area as a function of the number of accumulated frames under the influence of the collimating structure. The figure demonstrates that the maximum radius increases with the number of accumulated frames, although the rate of growth gradually decreases. Specifically, between 15 and 40 accumulated frames, the radius increases rapidly. Beyond 40 frames, the growth rate significantly slows, with the radius expanding from 720 to 740 units as the number of frames increases from 40 to 100. From 100 to 160 frames, the radius growth nearly halts.

This trend indicates that, initially, the accumulation of α particle response events leads to concentrated radiation energy deposition on the sensor, resulting in a rapid increase in the radius. This rapid initial growth reflects the sensor's high sensitivity to the initial radiation energy. As the number of accumulated frames increases, the system gradually approaches saturation, and the cumulative effect of response events diminishes, slowing the radius growth. This suggests that most active regions have been detected, and new response events contribute less to the radius. In the later stages, the system reaches a nearly balanced state, with minimal increases in α particle response events, resulting in almost no further growth in the radius.

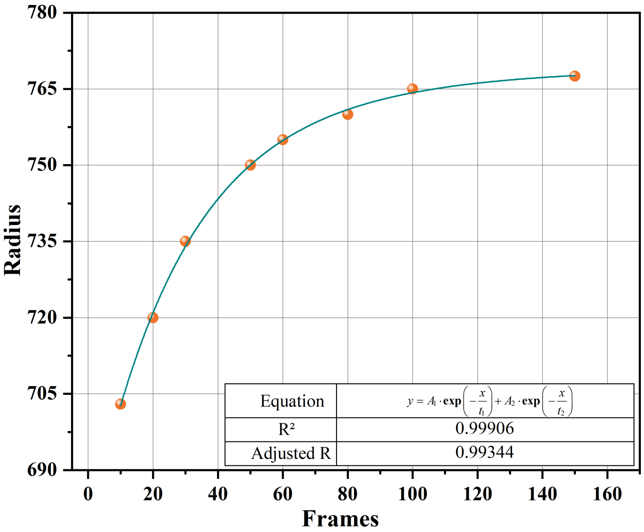

Fig. 7: Relationship between Frame Count and Radius

This phenomenon can be attributed to two factors. First, α particles scatter, and due to spatial angular effects, response signals from particles at the outer edges of one side of the detector originate from particles at the outermost edge on the opposite side of the radiation source. The longer travel distance and greater energy loss in the air result in fewer signals, leading to significantly fewer response signals at the outermost edges compared to the central region. Consequently, this phenomenon is not apparent when the number of frames is low but becomes more pronounced as the number of accumulated frames increases, causing the radius to grow. Therefore, under the influence of a collimating structure, the radius of the concentrated response event region can be considered constant.

Figure 8 illustrates the frame images of response events and the density distribution curves in the ring band region of figure 8b for different numbers of accumulated frames. As shown, the density variation of each ring band follows a consistent pattern: the density of response events increases as the distance from the center decreases. In the circular region with a radius of $0.2R$, the response event density reaches its maximum value. In the ring band between $0.2R$ and $0.4R$, although the density decreases, it remains relatively high. Over 40% of the response signals are concentrated within the circular region of radius $0.4R$, which accounts for only 16% of the total area. This indicates that, under the interference of the collimating structure, the radiation energy from the source is most concentrated in the central region, resulting in the highest density of response events near the center. This concentration occurs because α particles have limited penetration ability but strong ionization capability, causing most of their energy to be deposited in the central region. Additionally, the geometric concentration effect ensures that the central region occupies a symmetrical and concentrated spatial position, and the radiation energy propagates in a geometrically symmetrical manner, further enhancing the radiation density in the central region.

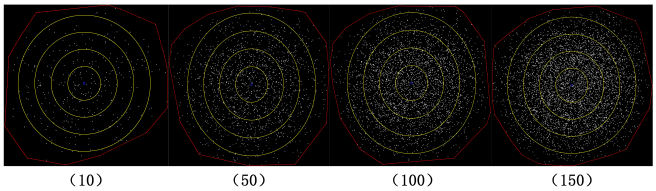

(a) Annular Distribution

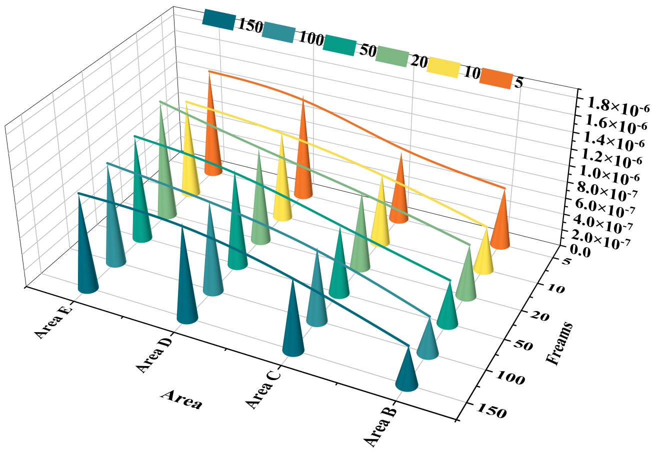

(b) The Relationship between Signal Density and Frame Count in Different Annular Bands

Fig. 8: Signal Density in Ring Band.

Figure 9 illustrates the variation of accumulated pixel values in different regions when the radiation source, positioned as shown in Figure 3a, irradiates the sensor under the influence of the collimation structure.

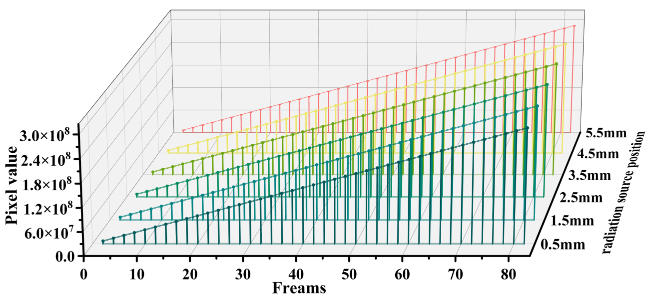

Fig. 9: The cumulative pixel values of the corresponding regions under different irradiation positions

As depicted in the figure, the irradiated regions exhibit a consistent response trend: as the number of accumulated frames increases, the accumulated pixel values in each region increase linearly, and the peak values across different regions are very similar. The linear increase in pixel values after stacking frames reflects the sensor's stable response to continuously incident particles. In each frame, the number of

particles and the energy deposition experienced by the sensor pixels remain constant, leading to the same pixel value increment per frame. This linear relationship indicates that the sensor's response to particle incidence is linear, meaning the output signal strength is directly proportional to the number of incident particles and their energy. Meanwhile, the similarity of peak values across regions demonstrates the spatial uniformity of the sensor's response. This implies that different regions of the sensor have similar response efficiencies under identical irradiation conditions. Therefore, separate calibration or compensation for different regions of the sensor is unnecessary. Thus, displacing the radiation source to different positions will produce consistent signal variations.

Figure 10 illustrates the nonuniformity distribution across different regions of the CMOS sensor when the radiation source is positioned at various irradiation points with the collimation structure in place. As depicted, when the radiation source directly irradiates a specific region of the sensor, the nonuniformity in that region reaches its maximum value. Although this maximum does not exceed 0.125, it is significantly higher than that in other regions.

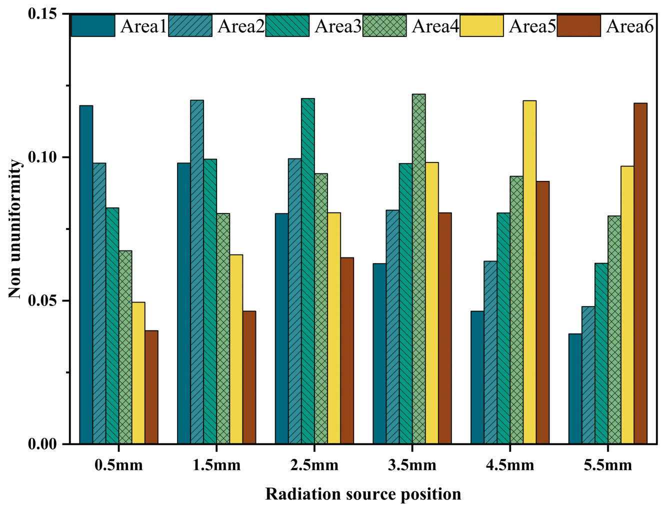

Fig. 10: Accumulated pixel values of the corresponding regions at different irradiation positions

The maximum difference in nonuniformity peak values between regions is less than 0.025, reflecting the overall consistency of the sensor's response.As the distance from the irradiated center increases, the nonuniformity in the regions gradually decreases. This trend occurs because the particle flux density decreases with increasing distance due to spatial diffusion and scattering effects. As particles propagate through the medium, they lose energy and change direction, leading to reduced energy deposition in regions farther from the center. This spatial distribution of energy deposition results in decreased nonuniformity.Moreover, this trend indicates that as the position of the radiation source changes, the energy deposition distribution in the irradiated region also changes, leading to variations in the nonuniformity distribution. The sensor can sensitively detect the movement of the radiation source by monitoring these changes. This demonstrates that under steady-state radiation field conditions, the CMOS sensor not only maintains a high degree of response uniformity but also exhibits high sensitivity and spatial resolution to changes in the radiation source position.

III. RADIATION SOURCE DISPLACEMENT MEASUREMENT METHOD

A. Measurement Method Based on Distribution Characteristics

Figure 11 shows the algorithm logic flowchart for source displacement judgment. As shown in the figure, a certain number of color images are first converted into dark images. After binarization of the dark images, morphological operations are performed to eliminate noise and obtain clean signal areas. Then, a connected component algorithm is used to identify the response signals in the image, and a curtain with the same size as the image is created to extract the response signals from frame i to frame $i+k$ and superimpose them to construct a point set. The centroid coordinates are calculated as:

$$(x, y) = \left(\frac{1}{n} \sum_{i=1}^{n} x_i, \frac{1}{n} \sum_{i=1}^{n} y_i \right)$$

The average distance d from the boundary to the centroid is determined, and circular regions with radii of $0.8d$, $0.6d$, $0.4d$, and $0.2d$ are divided. The signal concentration C in each annular region is calculated as:

$$C = \frac{N}{S}$$

where N is the number of response signals in the annular region and S is the area of the region. After processing all the images, the information (radius R, number of response signals N) of the annular region with the highest signal density is summarized. The average value of the radius R and the average number of response signals N are then calculated, and N_{mean} and R_{mean} are output.

DBSCAN algorithm is used to cluster the point set with R_{mean} as the optimal clustering radius and N_{mean} as the minimum sample size. The clusters and outliers are analyzed based on the geometric centroid position, and the entropy weight method is used to calculate the weight of each point. The entropy weight method first calculates the linear distance weight $w_l(p)$ and the density weight matrix $w_d(p)$ as:

$$w_l(p) = \max\left(0, 1 - \frac{\text{dist}(p, \text{centroid})}{R}\right)$$

where $w_l(p)$ is the position weight of the signal point p, $\text{dist}(p, \text{centroid})$ is the Euclidean distance from the signal point p to the cluster centroid, and R is the average distance

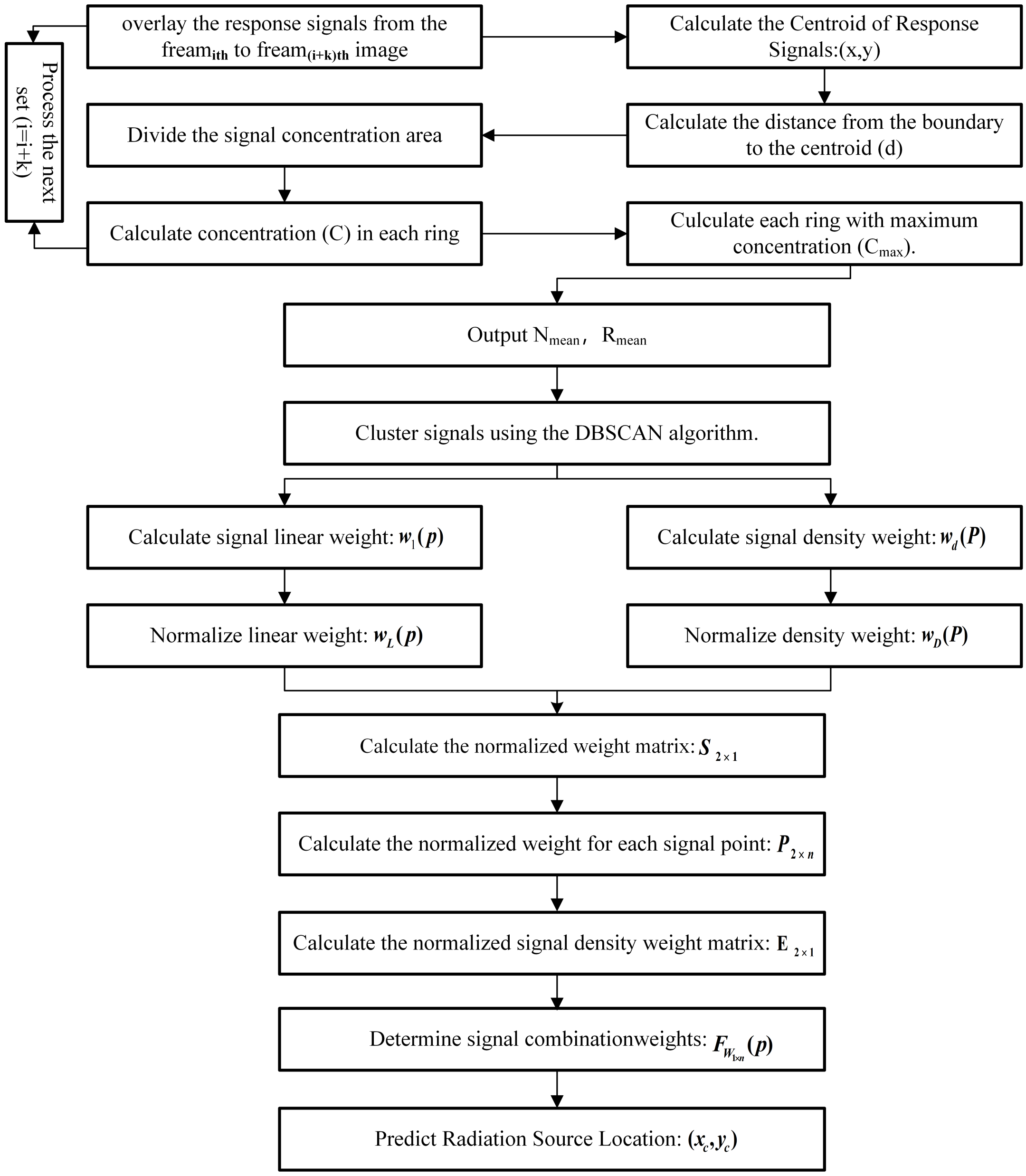

Fig. 11: Algorithm Flowchart

from all boundary points to the cluster centroid. The density weight $w_d(p)$ is defined as:

$$w_d(p) = \begin{cases} 5, & \text{if count}(p) \geq \text{density}_t \\ 0.5, & \text{otherwise} \end{cases}$$

where density_t is a density threshold. Next, the linear weight and density weight are normalized as:

$$w_r(p) = \frac{w_l(p) - w_{l\min}}{w_{l\max} - w_{l\min}}$$

$$w_L(p) = \frac{w_l(p) - w_{l\min}}{w_r(p)}$$

where $w_r(p)$ is the range of linear weight, $w_{l\max}$ and $w_{l\min}$ are the maximum and minimum values of the linear weight, and $w_L(p)$ is the normalized linear weight of each point. The density weight is similarly normalized.

After normalization, the entropy weight method is used to determine the combined weight, the normalized weight matrix $S_{2\times1}$, and the normalized proportion $P_{2\times n}$ of each signal point as:

$$S_{2\times1} = \sum T_{2\times n},\ \text{axis} = 1$$

$$P_{2\times n} = \frac{T_{2\times n}}{S_{2\times 1}}$$

where $S_{2\times 1}$ represents the sum of each weight, and $P_{2\times n}$ represents the normalized proportion of each signal point. The entropy value for the linear and density weights is then calculated:

$$K = \frac{1}{\log(n)}$$

$$E_{2\times 1} = -K \cdot \sum P_i \cdot \log(P_{2\times n} + 1e^{-10})$$

where P_i is the normalized proportion of each index and n is the number of signals. The entropy weight is then calculated from the entropy value:

$$F_W(p) = E_L \cdot W_L(p) + E_D \cdot W_D(p)$$

Finally, the weighted centroid positions (x_c, y_c) are computed as:

$$x_c = \frac{\sum_{i=1}^{n} F_i \cdot x_i}{\sum_{i=1}^{n} F_i}, \quad y_c = \frac{\sum_{i=1}^{n} F_i \cdot y_i}{\sum_{i=1}^{n} F_i}$$

where x_i, y_i are the coordinates of the i-th signal point and F_i is the final combined weight of the i-th signal point.

B. Empirical Experiment on Source Localization

Figure 12a presents a comparison of the average distance between the predicted and actual source positions using the traditional centroid method and the weighted centroid method at different numbers of accumulated frames. As shown, the prediction accuracy of both methods improves as the number of frames increases. This improvement occurs because a higher number of frames results in more detected alpha particle events, which reduces random errors and enhances the stability and reliability of the results.

In the traditional centroid method, when the number of frames is limited, particularly when it is below 20, the deviation between the predicted and actual source positions is large and exhibits significant fluctuations. The initial prediction error typically ranges from 30 to 45 pixels. This substantial error is caused by the radioactive source emitting alpha particles in all directions, combined with the limited number of particle events recorded within a single integration period, leading to an uneven spatial distribution of the signals.Additionally, the traditional centroid method assigns equal weight to all signals, neglecting differences in signal strength and spatial distribution. As a result, outliers, such as occasional pixels with high grayscale values, can have a significant impact on the centroid calculations. As the number of frames increases to 50, the prediction error starts to decrease and eventually stabilizes around 20 pixels. This improvement occurs because the increased number of particle events leads to a more uniform spatial distribution of the signals. Furthermore, as the sample size grows, the influence of outliers on the centroid calculation diminishes. However, the failure of the traditional centroid method to account for variations in signal strength and spatial distribution continues to limit its prediction accuracy.In contrast, the weighted centroid method demonstrates higher accuracy. When fewer than 20 frames are used, the error remains around 20 to 30 pixels; as the number of frames increases to 30, the error decreases further and eventually converges to approximately 8 pixels. This enhanced accuracy arises because the weighted centroid method effectively emphasizes high-intensity signal regions by assigning greater weight to pixels with higher signal strength, thereby biasing

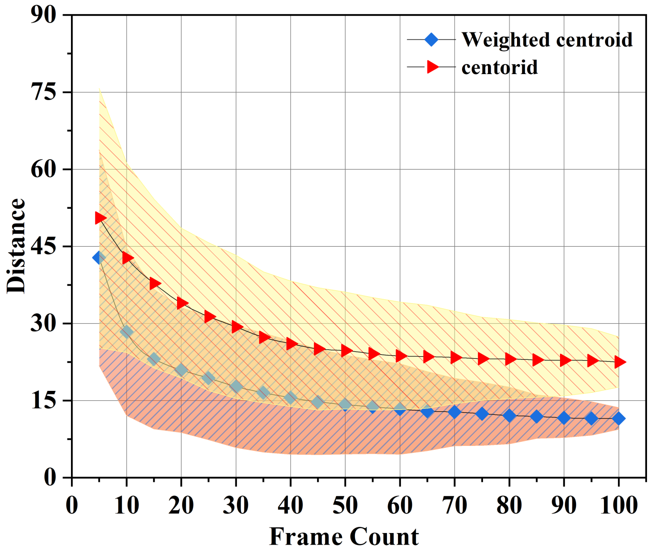

(a) Distance to Reference Point

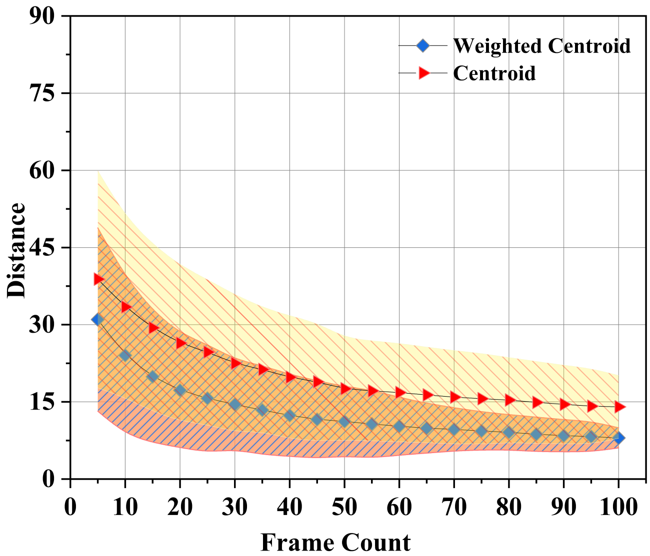

(b) Predicted Position Spacing

Fig. 12: Accuracy Comparison

the centroid calculation toward the true source location. Additionally, following the inverse square law, the weighted centroid algorithm assigns higher weights to signals closer to the center, further aligning the centroid calculation with the actual source position.

Figure 12b illustrates the dispersion of predicted source positions using both the weighted centroid and traditional centroid methods, evaluated across varying numbers of accumulated frames. As the number of frames increases, the predictions from both methods progressively converge, leading to enhanced stability in the results. Notably, the weighted centroid method yields more concentrated predictions and converges more rapidly compared to the traditional centroid method.For smaller frame counts, specifically when fewer than five frames are used, both methods exhibit comparable dispersion in the predicted source positions. This is attributed to the limited data points, which result in weak distribution characteristics of the response signals and obscure high-density regions. As the number of frames increases, the weighted centroid method demonstrates a faster convergence. When the frame count exceeds thirty, the average distance between predicted positions using the weighted centroid method stabilizes between 10 and 20 pixels.In contrast, the traditional centroid method maintains a larger average distance of approximately 40 to 60 pixels and shows greater error variability.Furthermore, the traditional centroid method tends to produce more dispersed predictions, particularly when the source is near the boundary of the region, which increases the likelihood of misjudgments. Once the number of frames exceeds fifty, the average distance for the traditional centroid method decreases slightly but stabilizes at a higher value, ranging from 20 to 30 pixels. This final value remains significantly greater than the convergence value observed for the weighted centroid method, highlighting the latter's superior accuracy and stability in source position prediction.

Figure 13 illustrates the maximum, minimum, and average distances between adjacent irradiation positions (spaced 1 millimeter apart) as predicted by the weighted centroid method under varying numbers of accumulated frames. As shown in the figure, with an increasing number of frames, both the maximum and minimum distances between adjacent predicted irradiation positions gradually converge toward the average predicted distance. Specifically, the maximum predicted distance decreases from 560 pixels to approximately 460 pixels, while the minimum distance increases from 300 pixels to about 420 pixels. The average distance is around 440 pixels, with an error of approximately 8 pixels compared to the actual irradiation positions.Additionally, the range of predicted distance variations progressively narrows, indicating that as the number of accumulated frames increases, the error between predicted and actual positions decreases, and prediction accuracy improves. The distribution range of the radioactive source's predicted positions also becomes narrower, converging from an initial spread of 260 pixels to 40 pixels. This improvement is attributed to the accumulation of frames, which clarifies the signal distribution characteristics and allows for a more rational allocation of signal weights, thereby reducing the distance between predicted and actual positions.

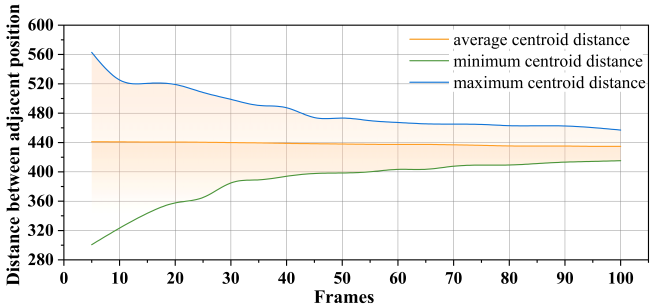

Fig. 13: Centroid Distances Between Adjacent Positions

C. Empirical Experiment on Source Displacement Direction Prediction and Measurement

Figure 14 shows the displacement and measurement verification results of the radioactive source moving in two different directions using the weighted centroid algorithm.

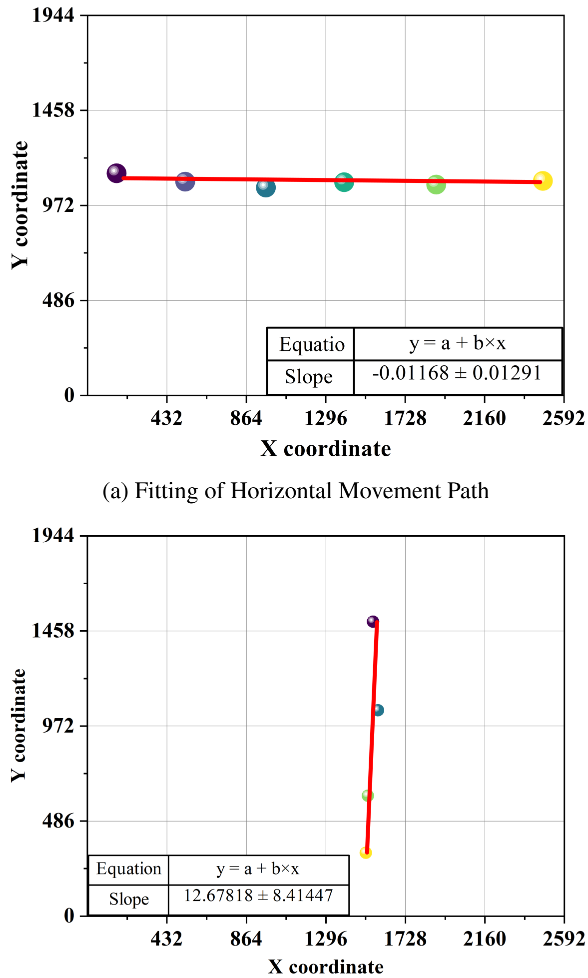

(a) Fitting of Horizontal Movement Path

(b) Fitting of Vertical Movement Path

Fig. 14: Trajectory Fitting of the Movement Paths

In Figure 14a, the radioactive source moves along the horizontal (X-axis) direction. The linear regression results indicate that the predicted path closely aligns with the actual movement path, with a regression slope of -0.0117. The angle error between the predicted and actual trajectories is $-0.68°$, demonstrating minimal position change along the Y-axis (vertical direction) during horizontal movement. This confirms that the algorithm can accurately capture the lateral displacement of the radioactive source. Figure 14b illustrates the movement of the radioactive source along the vertical (Y-axis) direction. The regression slope is 12.6782, and the angle error between the predicted and actual trajectories is $1.53°$, indicating a high degree of alignment between the predicted and actual paths.

Figure 15 illustrates the variation of centroid coordinates determined by the weighted algorithm during the uniform horizontal and vertical movements of the radioactive source. In the horizontal movement (Figure 15a), the slope is 421.3328, corresponding to an error of 11.6672 pixels in the movement speed. In the vertical movement (Figure 15b), the slope is -465.2105, with an error of 20.7895 pixels. In both directions, the algorithm predicts the displacement rate of the weighted centroid with an error of less than 5% compared to the actual displacement rate of the radioactive source.

IV. CONCLUSION

This paper presents a method for localizing and measuring the displacement of radioactive sources using CMOS active pixel sensors. By analyzing the response characteristics of active pixel sensors under varying α radiation irradiation conditions, we investigated the distribution patterns of response signals under collimator structure interference. Based on this analysis, we developed a displacement judgment and measurement method utilizing the weighted centroid algorithm, followed by experimental validation. The results demonstrate that:

The gray values of α particle response signals are predominantly concentrated between 150 and 255, typically comprising 3 to 8 high-gray-value pixels. These pixels exhibit a highly concentrated distribution pattern and respond uniformly across the entire pixel array. Regarding the distance between adjacent predicted positions, the maximum predicted distance decreases from 560 pixels to approximately 460 pixels, while the minimum distance increases from 300 pixels to about 420 pixels. The average distance is around 440 pixels, with an error of approximately 8 pixels compared to the actual irradiation positions.

When tracking a continuously moving radioactive source under low frame conditions, the predicted path closely aligns with the actual path. The angle of the predicted horizontal movement path is $0.01°$, and the linearity of the vertical movement path is $88.47°$. The angle error between the predicted and actual paths is less than 1.53%. Additionally, in both displacement modes, the predicted centroid displacement rate exhibits a small error relative to the actual displacement rate of the radioactive source, with errors below 5% of the actual movement speed. Specifically, the predicted horizontal movement speed is 421.3328 pixels, with an error of 11.6672 pixels compared to the actual displacement speed. The predicted vertical movement speed is -465.2105 pixels, with an error of 20.7895 pixels compared to the actual vertical speed. These results further validate the reliability and accuracy of the proposed method for judging radioactive source displacement.

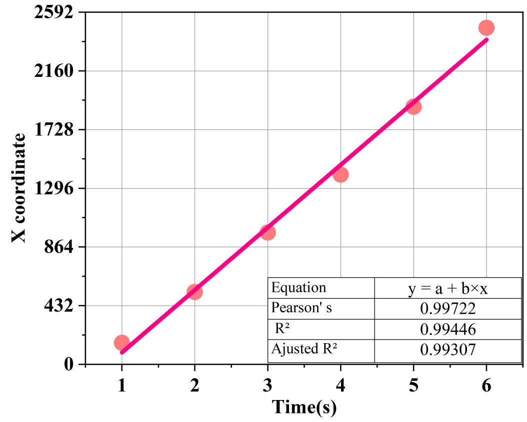

(a) Fitting of Horizontal Movement (X-Coordinate) with Time

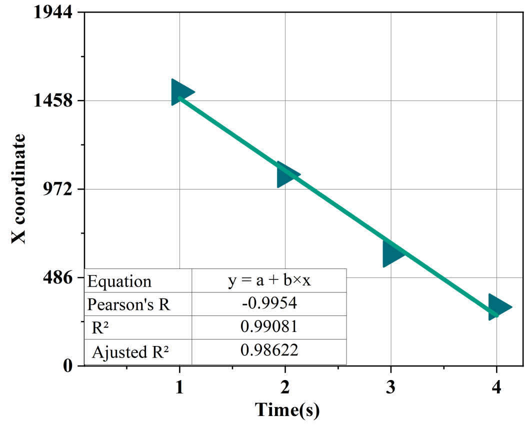

(b) Fitting of Vertical Movement (Y-Coordinate) with Time

Fig. 15: Fitting of Coordinates with Time

CMOS sensors offer excellent spatial resolution and uniform response characteristics. Utilizing the weighted centroid algorithm, the position of the radioactive source can be effectively predicted, and its movement direction and path can be accurately identified, demonstrating significant potential for future applications.

[1] Wei Q Y, Wang Z P, Dai T T, et al. Nuclear radiation detection based on un-covered CMOS camera under static scene. *Atomic Energy Science and Technology*, 2017, 51(1): 175-179.

[2] Zhang H, Liu Y, Wang L, et al. Nuclear radiation detection based on the convolutional neural network. *Physics*, 2022, 10(1): 1-9.

[3] Zhao Y, Liu M, Chen F, et al. Impact of irradiation damage to CMOS image sensor on camera performance. *Journal of Nuclear Optics*, 2023, 18(7): 101-109.

[4] Xu Shoulong, Zou Shuliang, Han Yongchao, et al. Ionizing radiation response uniformity of solid-state image sensors. *Acta Optica Sinica*, 2019, 39(7): 1-6.

[5] Liu Z, Wang P, Zhang H, et al. Effect of commercial off-the-shelf MAPS on -ray ionizing radiation response. *Sensors*, 2019, 19(22): 4950.

[6] Zhao Q, Liu Z, Wang J, et al. Random telegraph noises in CMOS image sensors caused by ionizing radiation. *IEEE Transactions on Nuclear Science*, 2019, 66(3): 1129-1135.

[7] Jones L, Smith D, Chen W, et al. CIS detectors for the auroral X-ray imaging. *Open Research Online*, 2019.

[8] Almeida BD, Amaro FD, Antonietti R, et al. Noise assessment of CMOS active pixel sensors for the CYGNO Experiment. *Measurement Science and Technology*, 2023.

[9] Ren W, Baudot J, Federici L, Finck C, et al. CMOS pixel sensors optimized for large ionizing dynamic. *Journal of Instrumentation*, 2022.

[10] Bugiel R, Bugiel S, Dannheim D, Fiergolski A, et al. High spatial resolution monolithic pixel detector in SOI technology. *Nuclear Instruments and Methods in Physics Research*, 2021.

[11] Moustakas K. Design and development of depleted monolithic active pixel sensors with small collection electrode for high-radiation applications. *IN2P3*, 2021.

[12] De Melo J, Deng W, Di Mauro A, et al. A compact front-end circuit for a monolithic sensor in a 65 nm CMOS imaging technology. *IEEE Transactions on Nuclear Science*, 2023.

[13] A hybrid global minimization scheme for accurate source localization based on signal attenuation. *IEEE Transactions on Signal Processing*, 2011.

[14] Aghasi H, Hashemi M, Khalaj B H. A source localization based on signal attenuation and time delay estimation in sensor networks. *Eurasip Journal on Advances in Signal Processing*, 2011, 81: 1-9.

[15] Kumar A, Abdelhakim A. Machine learning for localization of radioactive sources via a distributed sensor network. *Soft Computing*, 2023.

[16] Baca T, Stibinger P, Doubravova D, et al. Gamma radiation source localization for micro aerial vehicles with a miniature single-detector Compton event camera. *2021 International Conference on Unmanned Aircraft Systems (ICUAS)*.

[17] Lee MS, Anderson RB, Pehlivantürk C. Optimization strategies for Bayesian source localization algorithms. *IEEE Transactions on Nuclear Science*, 2022.